---

**Article:**
Li, Y., Liu, K., Wang, W. et al. (Accepted: 2025) Multi-State Asynchronous Joint Estimation for Lithium-Ion Batteries - A Nature Inspired Multi-Timescale Approach. IEEE transactions on industrial electronics (1982. Print). ISSN: 0278-0046 (In Press)

---

# Multi-State Asynchronous Joint Estimation for Lithium-Ion Batteries - A Nature Inspired Multi-Timescale Approach

Yihuan Li, Kaituo Liu, Wei Wang, Fang Fang, *Senior Member, IEEE*, Kailong Liu, *Senior Member, IEEE*, and Kang Li, *Senior Member, IEEE*

***Abstract*—Multi-state joint estimation enables more effective monitoring and assessment of battery operation conditions. This paper proposes a multi-timescale framework for asynchronous joint estimation of multiple coupled yet time-varying battery states, namely State of Charge (SOC), State of Energy (SOE), and State of Health (SOH). Firstly, an improved Convolutional Neural Network (CNN) architecture is designed to enhance the model feature extraction capability. Specifically, inception modules are integrated into the CNN model for long timescale feature extraction, while the feature map stacking combined with attention mechanisms is employed for short timescale feature extraction, leveraging the inherent multi-scale receptive fields of Inception to model global dependencies and the dynamic feature refinement capability of attention-enhanced stacking to emphasize local transient details. Secondly, a nature inspired r-GA optimization algorithm is proposed to enhance the training efficiency and performance of the CNN model by optimizing the network parameters. Besides, a Kalman filter is integrated to further improve the accuracy of state estimation by introducing physical information about the battery dynamics. Finally, the input dimensions and update strategies of the framework are tailored for different states to enable joint state estimation across multiple timescales. Experimental results demonstrate that the proposed framework produces much more precise estimation of SOC, SOE, and SOH with mixed-rate updates, while also exhibiting robustness when dealing with data corrupted with Gaussian white noise.**

***Index Terms*—Li-ion Batteries; Battery Management; Joint Estimation; Multi-Timescale Framework; Neural Networks**

## I. Introduction

LITHIUM-ION batteries (LIBs) have been widely used to support renewable integration and accelerate decarbonization of the transport and energy sectors due to their desirable properties on energy density and service life and ever decreasing costs [1]. To ensure the safe, efficient, and stable operation of the battery systems, precise state estimation is essential. Specifically, SOC, SOE, and SOH are three important states that respectively represent the remaining charge, endurance, and overall service life of a battery systems. Accurate state monitoring can help prolong battery lifetime and reduce the risk of system failures [2].

SOC and SOE are rapidly varying parameters that require real-time estimation to provide instantaneous information on battery charge and energy status [3]. Estimation methods for SOC and SOE can be broadly classified into model-based and data-driven methods [4]. Model-based methods (e.g., equivalent circuit models (ECM) and electrochemical models (EM) [5]) often face challenges in updating model parameters under varying operating conditions, whereas data-driven methods directly map measurable parameters to SOC/SOE using techniques such as CNNs [6], long short-term memory (LSTM) [7], [8], and gated recurrent unit (GRU) [9], enabling cross-battery adaptability.

SOH is an indicator to assess the degree of battery aging, and its estimation methods can be classified into direct and indirect methods [10]. Direct methods, such as DC and AC pulse-based internal resistance measurements and EIS-based impedance measurements, directly measure key physical quantities like resistance and impedance to assess the health status of LIBs. However, direct methods are not suitable for real-time applications, prompting increased attention to indirect methods, including model-based and data-driven-based approaches [11]. The rapid advancements in artificial intelligence have led to the growing prominence of data-driven-based approaches in this field, with methods like Physics-Informed Neural Network (PINN) [12] and BP neural network [13] demonstrating strong performance.

While the aforementioned studies have primarily focused on the analysis of a single battery state, an effective BMS necessitates integrated assessment and concurrent monitoring of multiple critical battery states, including SOC, SOE, and SOH. The joint estimation of these strongly coupled states facilitates more comprehensive state characterization, accurate performance assessment, and optimized management strate-

This work was supported by the National Natural Science Foundation of China (52307242, 62373224), in part by the Shenzhen Science and Technology Program (GJHZ20240218113404009), the Natural Science Foundation of Shandong Province (ZR2024JQ021), and the Fundamental Research Funds for the Central Universities (2025JC003). (Corresponding author: Kailong Liu.)

Yihuan Li, Kaituo Liu, Wei Wang and Fang Fang are with the School of Control and Computer Engineering, North China Electric Power University, Beijing, China (e-mail: yihuan@ncepu.edu.cn, kaituo@ncepu.edu.cn, wwang@ncepu.edu.cn, ffang@ncepu.edu.cn).

Kailong Liu is with the Shenzhen Research Institute of Shandong University, Shenzhen, China (e-mail: Kailong.Liu@email.sdu.edu.cn).

Kang Li is with the School of Electronic and Electrical Engineering, University of Leeds, UK (e-mail: K.Li1@leeds.ac.uk).

gies [14]. Understanding the interplay between these states is crucial. For instance, during battery aging, both capacity loss and reduced energy efficiency occur, leading to a decrease in the battery's ability to hold charge and store energy [15]. If the aging state of the battery is neglected and only SOC or SOE is estimated, the results may be biased. Therefore, to achieve reliable long-term predictions, joint estimation incorporating battery aging information is essential. For example, Song et al. [16] proposed a hybrid method that combines Least Squares Support Vector Machine (LS-SVM) and Unscented Particle Filter (UPF) to obtain the optimal estimates of SOC and SOH. Li et al. [15] developed a hybrid machine learning framework for joint SOC and capacity estimation, combining CNN with Gaussian Process Regression to generate mean and variance estimates of the states. Their experimental results demonstrate that incorporating battery aging information can significantly enhance the accuracy and reliability of SOC estimation. Moreover, since there is a high positive correlation between SOC and SOE, their joint estimation can enhance the stability of state estimation [17]–[19].

Overall, multi-state joint estimation presents significant advantages over single-state estimation and holds greater potentials in the development of advanced BMS. Although a variety of machine learning techniques have achieved success in joint battery state estimation, their potential for multi-timescale estimation remains underexplored. Given that SOH evolves gradually over long timescales, while SOE and SOC vary rapidly at short timescales, direct joint estimation without considering these temporal differences may lead to unnecessary computational overhead. Furthermore, many data-driven approaches may lead to suboptimal solutions due to the risk of getting trapped in local minima.

To address the above problems, this paper proposes a CNN-based multi-timescale framework for joint SOC, SOE and SOH estimation, employing specifically designed neural network architectures to capture their distinct dynamics and thus achieving real-time SOC/SOE tracking and periodic SOH updates. The main contributions of this study are as follows:

1) A novel multi-timescale framework that explicitly addresses the distinct temporal dynamics of SOH, SOC, and SOE through dedicated inputs and update strategies. This design enables synergistic estimation between the long-timescale SOH and short-timescale SOC-SOE modules.
2) A coherent structural design that integrates an input attention block with hierarchical feature fusion, via Inception layers or feature map stacking, and strategically replaces the flattening layer with global pooling. This synergy yields a compact, highly representative feature extractor with significantly reduced computational complexity.
3) A novel r-selection Genetic Algorithm (r-GA) featuring an expanded search space and enhanced optimization capabilities, specifically developed to ensure effective training of the proposed framework. This enhancement results in accelerated convergence and superior final performance.

## II. Proposed Multi-Timescale Estimation Framework

SOC, SOE, and SOH are important states of batteries that exhibit strong interdependence among them. Given that these states have distinct time-varying characteristics, this work proposes a multi-timescale framework to achieve accurate and synergistic estimation of SOC, SOE, and SOH. As illustrated in Fig.1, the proposed framework mainly consists of two key components: a long timescale estimation module for SOH estimation and a short timescale estimation module tailored for SOC and SOE estimation, considering that SOH changes slowly while SOC and SOE exhibit faster variations in real-time applications. Therefore, the input scale and update strategies are tailored for these two modules. This multi-timescale framework ensures accurate state estimation while reducing computational burden.

The main components of the proposed framework are detailed below.

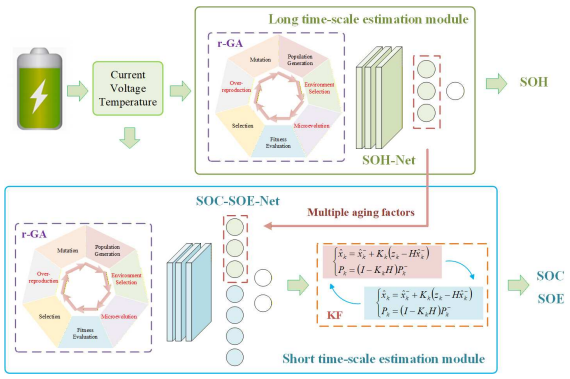


Fig. 1. Diagram of the multi-timescale joint estimation framework.

### A. Long Timescale Estimation Module

The long-timescale module designed SOH-Net, an enhanced CNN incorporating Inception blocks and global pooling to effectively capture long-term degradation dynamics from data at different scales.

On the one hand, SOH-Net must provide rapid responses to provide real-time aging factors for the short timescale estimation module. On the other hand, SOH estimation relies on long-term data to capture battery aging trends and provide accurate SOH predictions. Given these considerations, SOH-Net needs to process input data of varying sizes to meet different task requirements while ensuring accurate estimation results. To address these challenges, this study modifies the approach to extract one dimensional features for the CNN model, enabling SOH-Net to accept flexible input sizes. Additionally, Inception modules are incorporated into SOH-Net to enhance its feature extraction capability.

The architecture of SOH-Net is illustrated in the green box of Fig.2. The improved CNN architecture comprises convolutional layers, Inception block, global pooling layers, and fully connected layers. Traditional CNNs use the flatten layer to convert feature maps into one-dimensional (1D) vector, resulting in a large number of parameters in the fully

connected layers. SOH-Net improves this by incorporating an Inception module and global pooling for efficient 1D feature extraction. The Inception module leverages convolutional kernels of varying sizes and pooling operations to capture multi-scale features while avoiding a significant increase in computational cost. While, the global pooling layer reduces each feature map to a single value, substantially decreasing the number of model parameters while aggregating global information and mitigating the impact of local noise on feature extraction. Given that SOH estimation primarily relies on long-term aging trends rather than short-term local features, global pooling effectively captures global aging patterns without discarding critical information. This design not only reduces computational complexity but also preserves essential aging-related features, enhancing the model's robustness against noise.

Notably, the SOH-Net is designed to accommodate flexible input sizes through the use of global pooling to obtain 1D features, enabling it to perform various tasks across different timescales, from short-term aging factors updates to long-term SOH estimation. The length of input sequences is determined according to the different functions of this module.

When estimating SOC and SOE, SOC-SOE-Net requires SOH-Net to provide battery aging information in a timely and efficient manner. To maintain synchronization with SOC-SOE-Net, SOH-Net processes input matrix $X_K(m)$ constructed from short time-series and extracts aging features from $X_K(m)$ and feeds the output of the global pooling layer to SOC-SOE-Net, incorporating aging information into SOC and SOE estimation.

The raw data block $\mathcal{D}_K(m) \in \mathbb{R}^{m\times 3}$, containing historical measurements of three key battery parameters over the window $[K-m+1, K]$, is processed to generate input matrix $X_K(m)$ for SOH-Net to assess the aging state at time step $K$, where the transformation is defined as:

$$\mathcal{D}_K(m) = \begin{bmatrix} V_{K-m+1} & I_{K-m+1} & T_{K-m+1} \\ V_{K-m+2} & I_{K-m+2} & T_{K-m+2} \\ \cdots & \cdots & \cdots \\ V_K & I_K & T_K \end{bmatrix} \overset{transform}{\Rightarrow} X_K(m) \in \mathbb{R}^{\sqrt{m}\times\sqrt{m}\times 3} \quad (1)$$

where $V_K$, $I_K$, and $T_K$ represent the battery's voltage, current, and temperature measured at time $K$, respectively. In this study, the input matrix $X_K(m)$ is a three-dimensional (3-D) tensor with dimensions $\sqrt{m} \times \sqrt{m} \times 3$, where the first two spatial dimensions encode temporal proximity and the third dimension represents distinct battery parameters, facilitating efficient spatiotemporal feature extraction through convolutional processing while preserving inter-parameter correlations.

For SOH estimation, SOH-Net requires a relatively longer time-series $n$ to construct the input $X_K(n) \in \mathbb{R}^{\frac{n}{\sqrt{m}}\times\sqrt{m}\times 3}$, enabling it to capture the battery aging trend and provide accurate estimations. This design ensures consistent receptive fields for convolutional filters along the width dimension, enabling robust extraction of spatial features across varying height dimensions. This flexibility allows SOH-Net to provide aging factors to the SOC-SOE-Net and also obtain precise SOH estimates. The specific process for obtaining aging factors and estimating SOH is discussed in Section 2.4.

### B. Short Timescale Estimation Module

The short-timescale estimation module is centered around a specifically designed lightweight CNN, named SOC-SOE-Net, which is designed for the simultaneous estimation of SOC and SOE. As illustrated in the blue box of Fig. 2, its architecture employs attention-enhanced feature stacking—using an attention module, convolutional layers, and a channel-wise concatenation layer—to effectively extract salient short-term dynamics. A global pooling layer is introduced to reduce the computational complexity and a fully connected layer then generate the initial estimates. Subsequently, a Kalman filter refines these estimates by incorporating physical constraints. This hybrid design ensures real-time accuracy and temporal continuity of the estimation results. Furthermore, aging factors derived from the long-timescale module are integrated to preserve estimation accuracy under battery aging conditions.

Since the input consists of data of multiple time steps for different variables, the importance of individual features for SOC and SOE estimation varies significantly. Therefore, this study introduces an input attention block at the front of the SOC-SOE-Net to dynamically compute attention weights across the input data, selectively highlighting task-critical signals while attenuating noise and irrelevant elements. Specifically, a dual attention mechanism is employed in this block: temporal attention dynamically weights each time step's contribution by computing element-wise product between the attention matrix and input matrix, effectively capturing time-varying dynamics in battery operation, while channel attention adaptively weights each channel through learned feature interactions to quantify the relative contribution of different variables to the task. The attention weights are treated as trainable parameters in the network, which are adaptively adjusted during training.

Let the input data be $F \in \mathbb{R}^{H\times W\times C}$, where $H$ is the height, $W$ is the width, and $C$ is the number of channels. The output $F'$ of this attention block is calculated as follows:

$$F' = (W_t \odot (W_c \odot F)) \quad (2)$$

where $W_t \in \mathbb{R}^{H\times W}$ represents the time attention weights and $W_c \in \mathbb{R}^{C}$ represents the channel attention weights. The symbol $\odot$ denotes element-wise multiplication applied either channel-wise or position-wise. The input attention block can allocate attention to the input data with minimal computational cost.

At the tail of the SOC-SOE-Net, a hierarchical feature fusion strategy is employed to effectively combine multi-level features with controlled parameter overhead. This is achieved by stacking the feature maps from the three convolutional layers along the channel dimension, followed by a global pooling layer that condenses them into a compact 1D vector. This design efficiently generates a powerful fused representation by structurally replacing the parameter-heavy flattening operation with a more parameter-efficient global pooling operation.

Battery aging progressively degrades key parameters including capacity, internal resistance, and efficiency, leading to

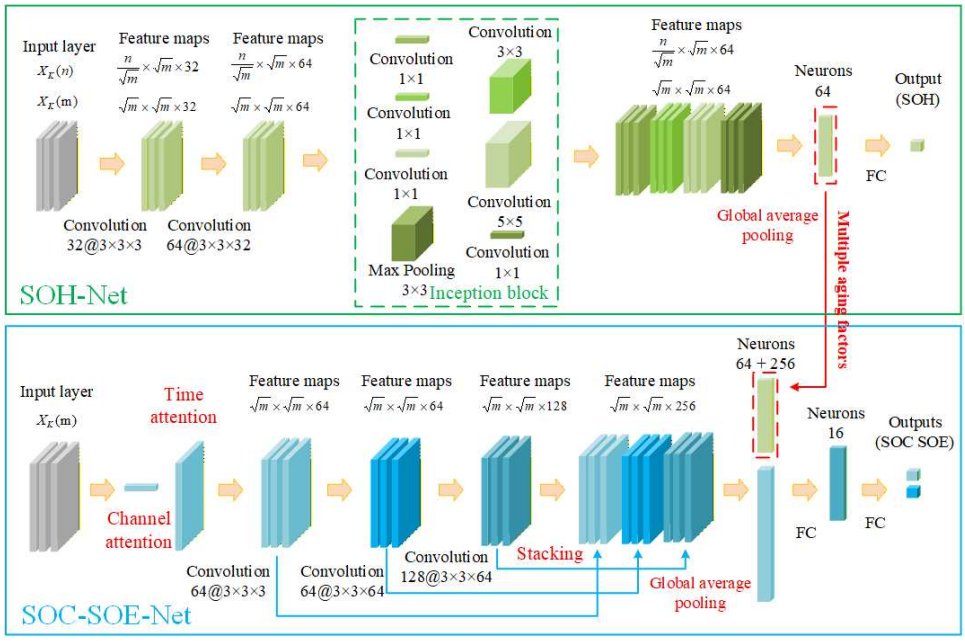


Fig. 2. Diagram of the network architecture for multi-timescale joint battery state estimation.

complex changes in its discharge curve. To further improve the estimation accuracy of SOC and SOE, this study integrates 1D aging factors extracted by the SOH-Net into the SOC-SOE-Net. The SOH-Net, designed for battery aging assessment with multi-scale feature extraction capabilities, captures more comprehensive aging-related factors than the SOC-SOE-Net, with these factors encoding richer degradation information than a single SOH value. Therefore, by concatenating these aging factors into the fully connected layer, the SOC-SOE-Net adaptively corrects aging-induced estimation biases and thus enhances estimation accuracy under aging conditions.

At time step $K$, SOC-SOE-Net uses data from time instant $K-m+1$ to time step $K$ and the aging factors provided by SOH-Net to predict the SOC and SOE at time step $K$. Without temporal modeling (e.g., recurrent connections), the SOC-SOE-Net's point estimation results at adjacent time steps may exhibit statistical independence [20]. To resolve this limitation and embed physical constraints into the data-driven estimates, a state-space model is formulated, detailed in (3) and (4). The state vector $\boldsymbol{S}_k = [SOC_k, SOE_k]^T$ evolves through Coulomb counting-based state functions, while the measurement vector $\boldsymbol{y}_k = [NN_{k,SOC}, NN_{k,SOE}]^T$ is the output SOC and SOE of the SOC-SOE-Net at time step $k$. A Kalman filter is then employed to optimally fuse these two complementary sources, whereby the physical state equations enforce current-integration constraints to achieve temporal smoothness, while the data-driven estimates from the SOC-SOE-Net provide the accuracy for correcting the prediction, thereby ensuring physically plausible and accurate estimation. The state evolution and measurement functions are given by:

$$\begin{cases} SOC_k &= SOC_{k-1} - \frac{I_k \Delta t}{C} + \omega_{SOC,k} \\ SOE_k &= SOE_{k-1} - \frac{I_k U_k \Delta t}{E} + \omega_{SOE,k} \end{cases} \tag{3}$$

$$\begin{cases} NN_{k,SOC} &= SOC_k + \nu_{k,SOC} \\ NN_{k,SOE} &= SOE_k + \nu_{k,SOE} \end{cases} \tag{4}$$

where $I_k$ and $U_k$ represent the current and voltage at time step $k$. $C$ and $E$ represent the maximum available capacity and energy, respectively. The estimated SOH obtained from the SOH-Net is multiplied by the rated capacity and energy to derive these values. $\Delta t$ is the sampling interval, $\omega \sim N(0, Q)$ and $\nu \sim N(0, R)$ are Gaussian process noise and Gaussian measurement noise, respectively.

### C. Joint State Estimation via Cross-module Feature Fusion

The proposed framework employs state-specific update strategies tailored to the temporal characteristics of each state. Specifically, the short timescale estimation module is updated at every time step to enable real-time tracking of SOC and SOE. While the long timescale estimation module operates in two distinct modes: a real-time auxiliary mode updated synchronously with the short timescale estimation module to provide instantaneous aging factors for real-time compensation of SOC and SOE estimates, and a periodic health assessment mode activated once per cycle to deliver a precise SOH estimate using accumulated operational data. This dual-strategy ensures both responsive SOC/SOE estimation with aging compensation and reliable long-term SOH assessment.

Assuming that the first $m$ time steps of a cycle are completed at time step $K$, SOH-Net performs to provide the aging factors, while SOC-SOE-Net is updated to estimate the SOC and SOE. At time step $K$, the aging factors $\mathrm{F}_a(K)$ are extracted by SOH-Net's layers before the fully-connected layer, as expressed by:

$$\mathrm{F}_a(K) = \mathrm{GP}\left(\mathrm{Inc}\left(\mathrm{Conv}(\mathrm{Conv}(X_K(\mathrm{m})))\right)\right) \tag{5}$$

where $\mathrm{Conv}(\cdot)$ represents the convolution operation, $\mathrm{Inc}(\cdot)$ represents the Inception module, $\mathrm{GP}(\cdot)$ represents the global pooling, and $X_K(m)$ represents the input data at time $K$.

For SOC-SOE-Net, a 1D feature is finally produced by the global pooling layer:

$$C_1 = \mathrm{Attn}(X_K(\mathfrak{m})) \tag{6}$$

$$C_2 = \mathrm{Conv}(C_1) \tag{7}$$

$$C_3 = \mathrm{Conv}(C_2) \tag{8}$$

$$\mathrm{F}_{\mathrm{SOC-SOE}}(K) = \mathrm{GP}\left(\mathrm{Concat}(C_1, C_2, C_3)\right) \tag{9}$$

where $C_1$, $C_2$, and $C_3$ denote the intermediate feature representations extracted at different stages of the network. Specifically, $\mathrm{Attn}(\cdot)$ represents the attention mechanism, and $\mathrm{Concat}(\cdot)$ represents the concatenation operation along the channel dimension. Finally, $\mathrm{F}_{\mathrm{SOC-SOE}}(K)$ denotes the extracted 1D feature at time $K$.

Subsequently, $\mathrm{F}_a(K)$ and $\mathrm{F}_{\mathrm{SOC-SOE}}(K)$ are concatenated and input into the fully connected layer of the SOC-SOE-Net:

$$\boldsymbol{y}_K = \mathrm{FC}\left(\mathrm{FC}\left(\mathrm{Concat}(\mathrm{F}_a, \mathrm{F}_{\mathrm{SOC-SOE}}(K))\right)\right) \tag{10}$$

where $\mathrm{FC}(\cdot)$ represents the fully connected layer. During other moments within the cycle, the SOC-SOE-Net continues performing real-time updates, while the SOH-Net utilizes the same short-term sequence data to provide aging factors in real time.

Data collection proceeds until $n$ time steps are accumulated as input, denoted as $X_{K-m+n}(n)$, which is then fed into the SOH-Net to obtain the SOH information for the corresponding cycle.

### D. r-GA Optimized Parameter Initialization

To mitigate the instability in model performance caused by poor parameter initialization in network training, a nature inspired genetic algorithm (GA) with r-selection strategy is proposed to evolve the initial parameter distribution of SOH-Net and SOC-SOE-Net, enabling the models to escape local optima in the initialization space compared to traditional initialization methods.

The global search capability of GA is positively correlated with population size. However, an excessively large population can lead to high computational costs and reduced search efficiency. To address this trade-off, this study draws on the principles of the r-selection strategy—part of the r/K selection theory in ecology [21], which describes a biological strategy characterized by high reproductive rates and rapid adaptation in high-mortality or unstable environments. Based on this concept, two key improvements are introduced to the GA, as shown in Fig.3, enabling it to maintain a relatively large population size while preserving high search efficiency.

Firstly, to enhance population diversity while preserving elite solutions, over-reproduction and environmental selection are proposed and integrated into the GA. By adopting an over-reproduction strategy, the reproduction rate and mutation rate are increased to ensure that each generation produces a large number of individuals, thereby enhancing population diversity and covering a broader search space. However, over-reproduction leads to a substantial population size in each

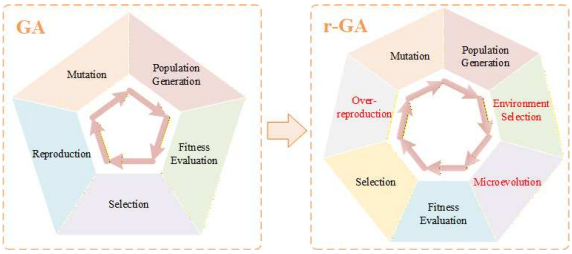


Fig. 3. Schematic diagram of structural improvements from GA to r-GA.

generation, and directly performing fitness evaluations and reproduction on such a large population would incur significant computational costs. To address this, an environmental selection function, is introduced to filter the population. This function eliminates most individuals at a relatively low computational cost, retaining only high-quality individuals for fitness evaluation and reproduction. While adding a modest computational overhead, this improvement greatly increases the likelihood of identifying the global optimal solution.

Besides, in nature, organisms gradually modify their traits between generations to adapt to environmental pressures. Therefore, microevolution is introduced into the GA by applying gradient descent to update the parameters of these individuals, allowing them to undergo small-scale evolution through one or several iterations.

To further clarify the stages of the nature inspired r-GA optimization pipeline, the corresponding calculations for each step are provided below:

1. Population Initialization: The r-GA initialization generates an initial population as:$P^{(0)} = \left\{\boldsymbol{x}_i^{(0)}\right\}_{i=1}^{N}$, where each individual $\boldsymbol{x}_i^{(0)} \in \mathbb{R}^d$ encodes the complete set of trainable parameters in the network, with $d$ being the total count of parameters. $N$ denotes the population size, indicating that there are $N$ different model parameter initialization configurations.

2. Environmental Selection: Each individual $\boldsymbol{x}_i^{(t)} \in P^{(t)}$ is evaluated by loading its parameters into the model and computing the loss on a small-scale environment screening dataset, using the loss function as the environmental selection function. This approach efficiently identifies high-quality individuals with low computational cost. The environmental selection function for an individual is computed as follows:

$$ES\left(\boldsymbol{x}_i^{(t)}\right) = \frac{1}{M}\sum_{j=1}^{M}\left(y_j - \hat{y}_j\left(\boldsymbol{x}_i^{(t)}\right)\right)^2 \tag{11}$$

where $M$ denotes the number of samples in the environment screening dataset, $y_j$ represents the true label of the j-th sample, and $\hat{y}_j\left(\boldsymbol{x}_i^{(t)}\right)$ denotes the prediction on sample $j$ using parameters from $\boldsymbol{x}_i^{(t)}$. A smaller $ES(\boldsymbol{x}_i^{(t)})$ value indicates a higher-quality individual $\boldsymbol{x}_i^{(t)}$. $k$ individuals with minimal $ES(\boldsymbol{x}_i^{(t)})$ values are selected, as expressed below:

$$S^{(t)} = \left\{\boldsymbol{x}_i^{(t)} \in P^{(t)} | rank(ES\left(\boldsymbol{x}_i^{(t)}\right) \leq k)\right\} \tag{12}$$

where $S^{(t)}$ is the selected subpopulation, and $rank(\cdot)$ assigns ascending ranks based on $ES(\boldsymbol{x}_i^{(t)})$ values.

3. Microevolution: First, an individual fitness function $f\left(\boldsymbol{x}_i^{(t)}\right)$ is introduced to evaluate the adaptability of an individual $\boldsymbol{x}_i^{(t)}$ within the population $S^{(t)}$, which reflects the impact of the corresponding parameter combination on the performance of the neural network. The fitness function is given by:

$$f\left(\boldsymbol{x}_i^{(t)}\right) = \frac{1}{V}\sum_{j=1}^{V}\left(y_j - \widehat{y}_j\left(\boldsymbol{x}_i^{(t)}\right)\right)^2 \tag{13}$$

The parameters of individual $\boldsymbol{x}_i^{(t)}$ are loaded into the model, and the loss function on the validation set is used as the fitness function. Here, $V$ represents the number of samples in the validation set. It is important to note that, a smaller fitness value in this context indicates better individual performance.

Inspired by the biological principle that organisms gradually alter their traits across generations to adapt to environmental pressures, this study proposes an individual parameter microevolution method based on the gradient descent algorithm. This method updates the parameters of an individual through one or multiple iterations, as expressed by

$$\boldsymbol{x}_i^{(t,e)} = \boldsymbol{x}_i^{(t)} - \eta\nabla f\left(\boldsymbol{x}_i^{(t)}\right), i = 1, 2, ..., k \tag{14}$$

where $\boldsymbol{x}_i^{(t,e)}$ is the evolved individual, $\nabla f\left(\boldsymbol{x}_i^{(t)}\right)$ represents the gradient of the fitness function at $\boldsymbol{x}_i^{(t)}$, and $\eta$ is the learning rate controlling the update step size.

4. Fitness Evaluation: The fitness of individuals that have undergone environmental selection and microevolution is evaluated using $f\left(\boldsymbol{x}_i^{(t,e)}\right)$.

5. Selection: Individuals are selected for reproduction based on their fitness:

$$P\left(\boldsymbol{x}_i^{(t,e)}\right) = \frac{\frac{1}{f\left(\boldsymbol{x}_i^{(t,e)}\right)}}{\Sigma_{j=1}^{k}\left(\frac{1}{f\left(\boldsymbol{x}_j^{(t,e)}\right)}\right)} \tag{15}$$

where $P\left(\boldsymbol{x}_i^{(t,e)}\right)$ represents the probability of individual $\boldsymbol{x}_i^{(t,e)}$ reproducing, with the selection probability inversely proportional to its fitness in this study.

6. Over-reproduction: Following the r-selection strategy, a large number of individuals are generated through genetic recombination:

$$\boldsymbol{x}_{new}^{(t)} = \text{Crossover}\left(\boldsymbol{x}_i^{(t,e)}, \boldsymbol{x}_j^{(t,e)}\right) \tag{16}$$

where $\boldsymbol{x}_{new}^{(t)}$ denotes the new individual generated by recombining the genes of the selected individual.

7. Mutation

$$\boldsymbol{x}_{new}^{'(t)} = \boldsymbol{x}_{new}^{(t)} + \Delta\boldsymbol{x}_{new} \tag{17}$$

where $\boldsymbol{x}_{new}^{'(t)}$ represents a new individual generated by mutating part of the genes of $\boldsymbol{x}_{new}^{(t)}$, and $\Delta\boldsymbol{x}_{new}$ denotes the random disturbance.

8. Iteration: The individuals generated through mutation form the new generation population. The process iterates by repeating steps (2) to (7) until the termination condition is met. Once the termination condition is satisfied, the current optimal individual is output as the initial parameters of the neural network model.

## III. Dataset and Implementation Details

### A. Dataset Settings

As shown in Fig.4, the battery testing platform consists of lithium-ion batteries, a NEWARE BTS-4000 battery test system, and a data processor. Four commercial 18650 $LiFePO_4$ batteries are used in this work, each with a nominal voltage of 3.2 V and a nominal capacity of 1.6 Ah. All experiments were conducted at a temperature of 25°C. Batteries underwent Constant-Current Constant-Voltage (CC-CV) charging (1C to 3.6 V, then CV until current $\leq$ 75 mA) and Constant-Current (CC) discharging, with the discharge current set at 1C for the first 300 cycles (Stage 1) and 2C for the subsequent 600 cycles (Stage 2 and 3), respectively. A 10-minute rest period was included between each charge and discharge process. The collected data constitute Dataset 1, which serves as the primary dataset for analysis and comparative experiments.

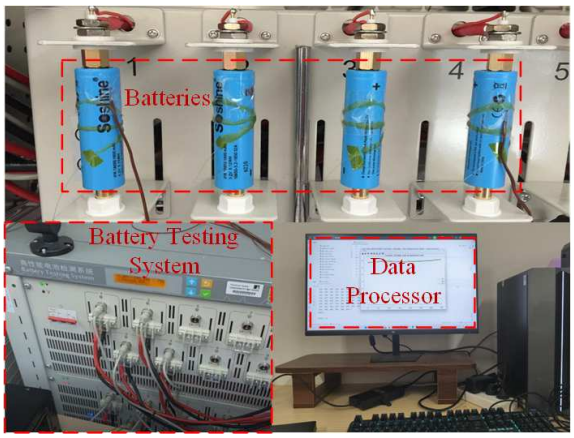


Fig. 4. Battery testing platform.

The Dataset 1 was split into training, validation, and testing sets. Data from three batteries was used for training, divided into a training set and a validation set at a ratio of 8:2. Additionally, 10% of the validation set was designated as the environmental screening dataset. Data from the remaining battery was used to construct the test set.

In addition, Dataset 2, derived from the Nickel Cobalt Aluminum (NCA) battery dataset [22], is used as a supplementary dataset to further evaluate the generalization capability and robustness of the proposed method. It comprises long-term cycling tests conducted at 25 °C, 35 °C, and 45 °C. The cycling protocol involved CC charging at current rates ranging from 0.25 C (0.875 A) to 1 C (3.5 A) until the voltage reached 4.2 V, followed by CV charging at 4.2 V until the current decreased to 0.05 C. Subsequently, the cells were discharged under a CC of 1 C until the voltage dropped to 2.65 V.

Dataset 2 includes 14 batteries tested under five operating conditions from the NCA dataset. The training set of Dataset 2 consists of 12 batteries under three operating conditions: “CY25-05_1”, “CY25-025_1”, and “CY45-05_1”, with data

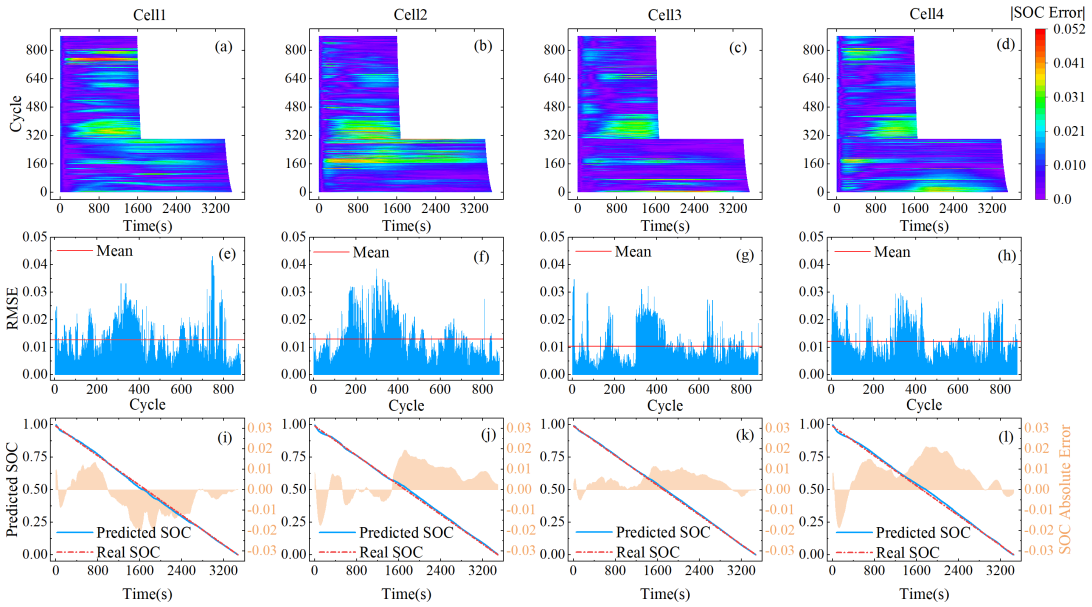


Fig. 5. SOC estimation results. (a)-(d) Absolute errors in SOC Estimation for Cell1, Cell2, Cell3 and Cell4. (e)-(h) RMSEs of SOC estimation for each cycle on Cell1, Cell2, Cell3 and Cell4. (i)-(l) SOC estimation curves for the 100th Cycle of Cell1, Cell2, Cell3 and Cell4.

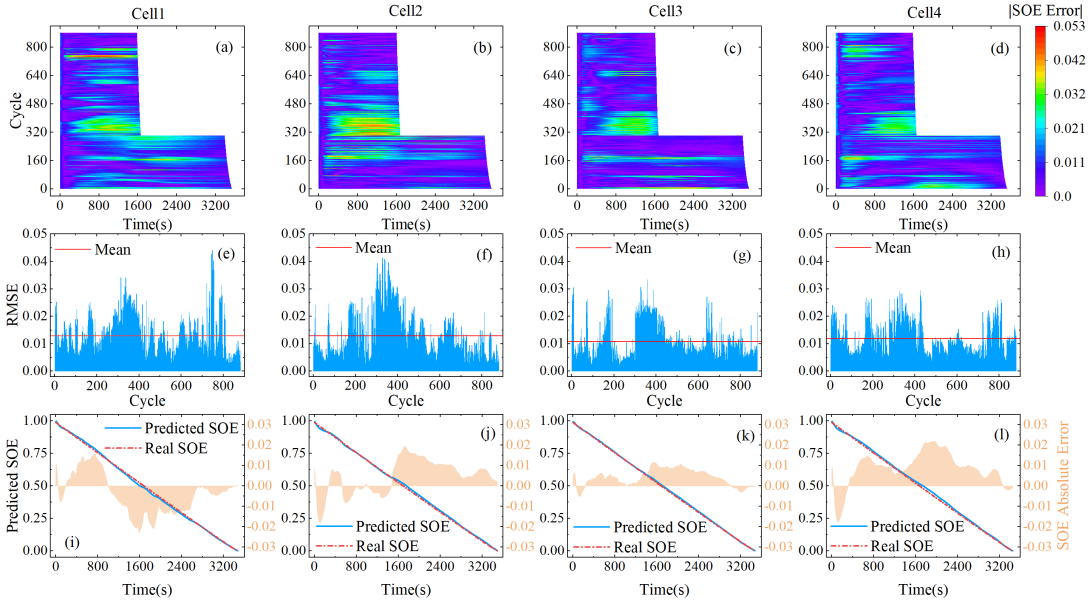


Fig. 6. SOE estimation results. (a)-(d) Absolute errors in SOE Estimation for Cell1, Cell2, Cell3 and Cell4. (e)-(h) RMSEs of SOE estimation for each cycle on Cell1, Cell2, Cell3 and Cell4. (i)-(l) SOE estimation curves for the 100th Cycle of Cell1, Cell2, Cell3 and Cell4.

partitioning consistent with Dataset 1. The test set includes cells under "CY25-1_1" and "CY35-05_1" conditions. Here, "CY25-05_1" denotes a test performed at 25 °C with a 0.5 C charging rate and a 1 C discharging rate. Since the sampling intervals in Dataset 2 were not uniform, the data were first interpolated to a fixed frequency of 1 Hz to maintain a consistent temporal resolution with Dataset 1.

### *B. Input Structure*

Two different scales of input samples, created for different purposes, are generated through data segmentation with different sliding window sizes.

First, a sliding window of length $m$ is applied with a stride of 1 to scan the entire normalized measurement data, generating multiple input matrices $X_K(m)$ as input samples. In this study, $m$ is set to 36, meaning that each input sample is a 3-D tensor of size $6 \times 6 \times 3$, representing the sequences of current, voltage, and temperature over 36 consecutive time steps. This short window is sufficient to capture the immediate battery dynamics while maintaining the low latency required for real-time operation. Each input sample is processed in a forward pass, with the SOH-Net using this sample to obtain aging factors, while the SOC-SOE-Net uses the same sample to estimate the SOC and SOE at the final time step of the input

sequence. All inputs consist solely of the measured voltage, current, and temperature data.

Next, a sliding window of length $n$ is applied in the same manner to extract input samples $X_K(n)$, with $n$ set to 360. This value was determined to provide a data window that is both long enough to be representative of a cycle's dynamics for accurate SOH inference, and short enough to ensure practical utility. Each $X_K(n)$ sample is a 3-D tensor of size $60 \times 6 \times 3$, maintaining the same width as $X_K(m)$. The corresponding output is the SOH of the cycle to which the $X_K(n)$ sample belongs. These $X_K(n)$ samples are exclusively used in SOH-Net for SOH estimation.

By constructing these fixed-length sequences, the proposed model is trained to be robust, ensuring accurate estimation at any intermediate points without reliance on a fixed initial state.

## IV. Experimental Results and Analysis

The performance of the proposed model is evaluated using Root Mean Square Error (RMSE), Mean Absolute Error (MAE), and Maximum Absolute Error (MAX). Unless otherwise specified, Dataset 1 was used by default for all evaluation and analysis.

### A. Joint estimation of SOC, SOE and SOH

Cross-validation techniques are employed to verify the feasibility of the multi-timescale joint estimation framework. The framework was trained using data from any three batteries, with the remaining battery data used as the test set.

The SOC estimation results for Cell 1-4 during the entire testing process are shown in Fig.5. From Fig.5(a)-(d), it can be observed that, in most cases, the absolute SOC estimation error for the four batteries remains below 1.5%. Fig.5(e)-(h) display the RMSEs of SOC estimation for each cycle, indicating that the RMSEs remain below 2% for most cycles. Fig.5(i)-(l) visualize the SOC estimation curves and error curves for the 100th cycle of each of the four batteries, showing that the estimated results closely match the actual results, with RMSE values of 0.98%, 0.956%, 0.595%, and 1.18%, respectively.

Due to the strong positive correlation between SOE and SOC, and since both are estimated by SOC-SOE-Net, the SOE estimation results are highly similar to those of SOC. Fig.6 shows the SOE estimation results for Cell 1-4 throughout testing. The absolute error mostly remains below 1.5% (Fig.6(a)-(d)), with only a few cycle RMSES exceeding 2% (Fig.6(e)-(h)). Fig.6(i)-(l) visualize the SOE estimation curves and error curves for the 100th cycle, demonstrating that the estimated results closely align with the actual results, with RMSE of 1.08%, 0.942%, 0.583%, and 1.19%, respectively.

For SOH estimation, the proposed framework maintains a high level of accuracy. Fig.7(a)-(d) show the SOH estimation results for Cell 1-4, with predicted values closely aligning with the actual values. The step-like fluctuations are primarily attributed to the experimental discontinuities. The most prominent step occurs around cycle 300, coinciding with the transition from Stage 1 (1C discharge) to Stage 2 (2C discharge) after a rest period of around two days. A less pronounced step near cycle 600 corresponds to the transition between Stages 2 and 3, which employed the same 2C discharge current and were likewise separated by a rest period of around two days. Furthermore, the limited aging depth and number of batteries challenge the learning of a smoother estimation curve. Despite this, the estimation errors for most cycles remain consistently within 3%, as shown in Fig.7(e)-(h), confirming the model's practical reliability. In Table I, the rows labeled 'Proposed' summarize the RMSE, MAE, and MAX values for SOC, SOE, and SOH estimations of Cell 1-4.

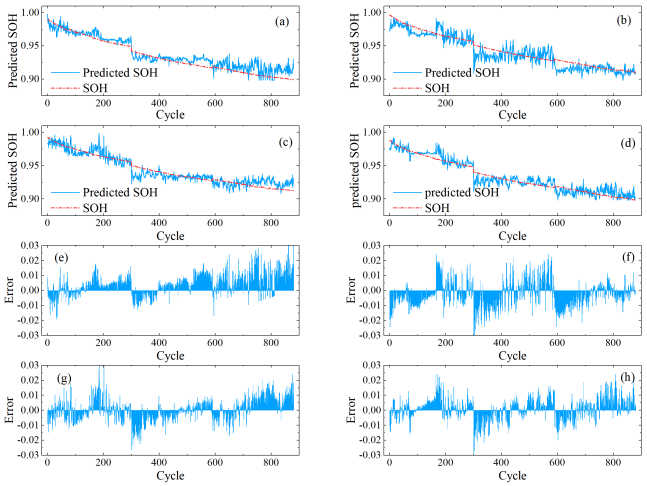


Fig. 7. SOH estimation results. (a)-(d) SOH estimation curves for Cell1-4. (e)-(h) SOH estimation errors for Cell1-4.

### B. Comparison with other state estimation models

In this section, several traditional networks were employed to separately estimate the SOC, SOE, and SOH for comparison with our proposed framework. These models include CNN, LSTM, and RNN [23]. All models utilized the same input data.

The comparative experimental results are presented in Table I, where our framework (labeled as 'Proposed' in Table I) achieves superior performance for most cases across all batteries. Notably, for Cell1, the SOC and SOE estimations using CNN, LSTM, and RNN exhibit significantly large MAX values, indicating the presence of outliers in Cell1's data that lead to considerable deviations in individual estimations. In contrast, our framework employs global average pooling to extract 1D features, which mitigates the impact of outliers on the estimation results. Additionally, the inclusion of an online Kalman filter further enhances the robustness of the estimations against interference.

In addition, to enable a fair and comprehensive comparison, several advanced methods for the joint estimation of SOC, SOE, and SOH were introduced, including N-BEATS, Transformer, Temporal Convolutional Network (TCN), and BiLSTM + UKF [24]–[28]. The comparative experimental results are summarized in Table II, where our framework consistently demonstrates superior performance across most cases for all tested batteries.

Furthermore, Table III summarizes the floating-point operations (FLOPs), number of parameters, and inference time of the joint estimation methods. Although the proposed framework exhibits relatively higher FLOPs due to processing two inputs of different shapes during a single inference, it achieves a shorter inference time.

Therefore, it can be concluded that the proposed framework attains high inference efficiency while maintaining superior estimation accuracy.

### C. Noise Testing

To evaluate the robustness of the proposed method, three types of noise were introduced into the dataset. These include one set of Gaussian noise and two sets of mixed non-Gaussian noises (NGNs) [29]. The NGN is constructed as $v_n = (1 - a_n)b_n^* + a_n c_n$, where $b_n^*$ represents the background noise. In this study, two types of background noise were simulated: Laplacian noise and uniformly distributed noise. $c_n$ denotes Gaussian noise, which is used to simulate outliers. $a_n$ is an independent and identically distributed binary process with a probability distribution of $Pr(a_n = 1) = p$ and $\Pr(a_n = 0) = 1 - p$, where $0 \leq p \leq 1$ represents the occurrence probability. In this study, $p$ was set to 0.001.

All three types of noise have a mean of zero and share the same standard deviation to ensure comparable noise intensity. Specifically, for the first set of Gaussian noise, the standard deviations of current, voltage, and temperature were set to $\sigma_i$, $\sigma_v$, and $\sigma_t$, respectively. For $b_n^*$, the standard deviations of current, voltage, and temperature were also set to $\sigma_i$, $\sigma_v$, and $\sigma_t$, while for $c_n$, the standard deviation was set to ten times that of the corresponding channel.

The values of these parameters were systematically adjusted to assess the model's performance under different noise intensities. The detailed parameter settings are summarized in Table IV.

Fig.8 illustrates the variation in RMSE for SOC and SOE estimations on Cell4 across different models as the noise intensity increases under three noise types. As the noise level rises, the RMSEs of SOC and SOE in the proposed framework exhibit only a slight increase, whereas those of other models increase substantially, demonstrating the superior noise resistance of the proposed framework.

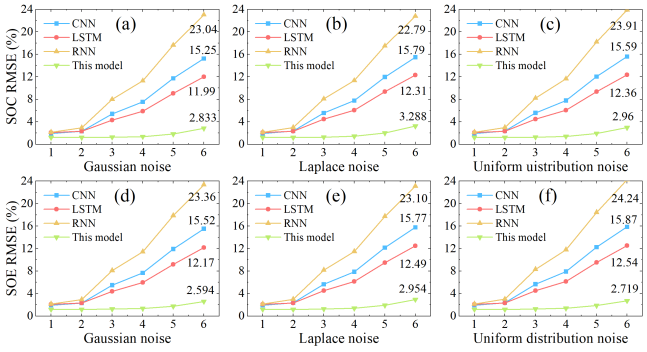


Fig. 8. Noise test results for Cell4 under different noise conditions with various models. (a)-(c) RMSE of SOC estimations. (d)-(f) RMSE of SOE estimations.

### D. Impact of Aging Factors on SOC and SOE Estimation

To assess the impact of incorporating aging factors on SOC and SOE estimation, experiments using models without aging factors are conducted as a baseline for comparison. Estimation performance is evaluated under varying levels of battery degradation. Specifically, the data from Cell4 is randomly selected as the test set, while the data from the remaining cells is used for training. As shown in Fig.9, during the initial 600 cycles, when the battery remains in good health, the inclusion of aging factors has minimal effect on SOC and SOE estimation. However, during the final approximately 200 cycles, the average RMSEs of SOC and SOE estimations decreased by 55.76% and 61.59%, respectively, with the introduction of aging factors. This demonstrates that the inclusion of the aging factors allows the SOC-SOE-Net to focus more on the aging state of the battery, providing more reliable long-term estimations.

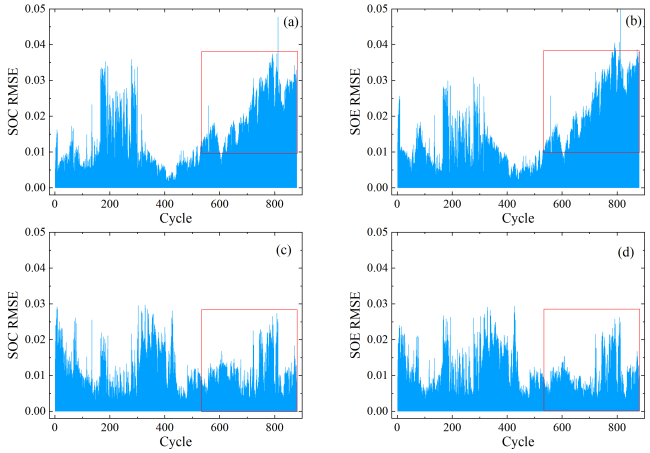


Fig. 9. Impact of aging factors on estimation accuracy. (a-b) RMSE of SOC/SOE estimation without aging factors. (c-d) RMSE of SOC/SOE estimation with aging factors.

### E. Supplementary experiments

To further validate the performance of the proposed framework, additional experiments were conducted using Dataset 2. Since Dataset 2 does not include energy data, only SOC and SOH were predicted. However, given the strong correlation between SOC and SOE, accurate SOC estimation also implies reliable SOE prediction performance.

The SOC estimation results are presented in Fig.10. For "CY25-1_1", the absolute errors across all samples were mostly below 3.0%, and the RMSE for each cycle remained under 3.6%. As "CY25-1_1" undergoes aging, the RMSE gradually increases, primarily because this cell experiences significant degradation within only 28 cycles, leading to a noticeable deviation from the aging trend of the training data. Nevertheless, the proposed framework still achieves reliable state estimation for this cell. For "CY35-05_1", the absolute errors were mostly below 1.6%, with cycle-wise RMSE values below 1.7%. Furthermore, the SOC estimation curves of the first cycle for both cells show that the predicted values closely

TABLE I
RMSEs, MAEs AND MAXs OF SOC, SOE, AND SOH ESTIMATIONS WITH DIFFERENT SINGLE-STATE ESTIMATION MODELS (IN %).

| Battery | Model | SOC | | | SOE | | | SOH | | |
|---|---|---|---|---|---|---|---|---|---|---|
| | | RMSE | MAE | MAX | RMSE | MAE | MAX | RMSE | MAE | MAX |
| Cell1 | CNN | 1.723 | 1.339 | 21.69 | 1.738 | 1.349 | 22.21 | 1.229 | 0.964 | 3.928 |
| | LSTM | 1.642 | 1.223 | 18.90 | 1.663 | 1.229 | 19.34 | 1.159 | 0.966 | 3.697 |
| | RNN | 1.755 | 1.304 | 24.52 | 1.781 | 1.313 | 25.06 | 1.115 | 0.903 | 3.575 |
| | Proposed | **1.269** | **1.149** | **5.143** | **1.288** | **1.167** | **5.257** | **0.878** | **0.695** | **3.149** |
| Cell2 | CNN | 1.650 | 1.298 | 9.359 | 1.684 | 1.316 | 9.623 | 1.497 | 1.184 | 4.769 |
| | LSTM | 1.718 | 1.319 | 7.955 | 1.752 | 1.336 | 8.029 | 1.156 | 0.899 | **3.366** |
| | RNN | 1.586 | **1.200** | 8.272 | 1.621 | 1.217 | 8.355 | 1.299 | 0.998 | 5.387 |
| | Proposed | **1.296** | 1.221 | **5.147** | **1.287** | **1.122** | **5.074** | **0.956** | **0.768** | 4.200 |
| Cell3 | CNN | 1.614 | 1.247 | 7.111 | 1.612 | 1.243 | 7.213 | 1.083 | 0.825 | 4.358 |
| | LSTM | 1.541 | 1.136 | 7.894 | 1.550 | 1.143 | 8.126 | 0.941 | 0.704 | 6.679 |
| | RNN | 1.629 | 1.207 | 10.40 | 1.627 | 1.207 | 10.71 | 0.972 | 0.721 | 5.820 |
| | Proposed | **1.034** | **0.848** | **4.481** | **1.072** | **0.903** | **4.675** | **0.789** | **0.618** | **3.426** |
| Cell4 | CNN | 1.911 | 1.518 | 11.10 | 1.910 | 1.507 | 11.37 | 1.130 | 0.933 | 3.541 |
| | LSTM | 2.105 | 1.608 | 10.22 | 2.085 | 1.581 | 10.30 | 1.141 | 0.931 | 3.858 |
| | RNN | 2.165 | 1.642 | 10.50 | 2.152 | 1.612 | 10.62 | 1.134 | 0.924 | 3.286 |
| | Proposed | **1.210** | **1.053** | **4.934** | **1.185** | **1.044** | **4.834** | **0.756** | **0.581** | **2.914** |

TABLE II
RMSEs, MAEs AND MAXs OF SOC, SOE, AND SOH ESTIMATIONS WITH DIFFERENT MULTI-STATE JOINT ESTIMATION METHODS (IN %).

| Battery | Model | SOC | | | SOE | | | SOH | | |
|---|---|---|---|---|---|---|---|---|---|---|
| | | RMSE | MAE | MAX | RMSE | MAE | MAX | RMSE | MAE | MAX |
| Cell1 | N-BEATS | 1.831 | 1.380 | 18.605 | 1.831 | 1.369 | 19.097 | 1.260 | 1.045 | 5.655 |
| | Transformer | 1.937 | 1.531 | 19.354 | 1.986 | 1.557 | 20.075 | 1.297 | 1.059 | 4.074 |
| | TCN | 2.084 | 1.559 | 19.728 | 2.125 | 1.587 | 20.205 | 1.297 | 1.024 | 3.793 |
| | BiLSTM + UKF | 1.352 | 1.151 | 11.704 | 1.380 | **1.161** | 12.117 | 1.228 | 0.993 | 5.331 |
| | Proposed | **1.269** | **1.149** | **5.143** | **1.288** | 1.167 | **5.257** | **0.878** | **0.695** | **3.149** |
| Cell2 | N-BEATS | 1.765 | 1.314 | 11.344 | 1.777 | 1.330 | 11.478 | 1.397 | 1.079 | 5.449 |
| | Transformer | 1.724 | 1.294 | 9.593 | 1.690 | 1.300 | 8.989 | 1.720 | 1.346 | 4.994 |
| | TCN | 2.142 | 1.594 | 12.656 | 2.189 | 1.623 | 13.050 | 1.583 | 1.266 | 4.860 |
| | BiLSTM + UKF | 1.462 | 1.259 | 9.327 | 1.480 | 1.279 | 9.335 | 1.414 | 1.072 | 4.465 |
| | Proposed | **1.296** | **1.221** | **5.147** | **1.287** | **1.122** | **5.074** | **0.956** | **0.768** | **4.200** |
| Cell3 | N-BEATS | 2.003 | 1.497 | 9.390 | 1.913 | 1.417 | 9.324 | 1.132 | 0.879 | 6.219 |
| | Transformer | 1.523 | 1.250 | 10.086 | 1.501 | 1.231 | 10.322 | 0.985 | 0.746 | 5.262 |
| | TCN | 1.436 | 1.114 | 7.353 | 1.509 | 1.190 | 7.914 | 0.919 | 0.687 | 5.020 |
| | BiLSTM + UKF | 1.816 | 1.426 | 12.123 | 1.842 | 1.436 | 12.557 | 1.012 | 0.763 | 5.483 |
| | Proposed | **1.034** | **0.848** | **4.481** | **1.072** | **0.903** | **4.675** | **0.789** | **0.618** | **3.426** |
| Cell4 | N-BEATS | 1.997 | 1.568 | 10.381 | 2.012 | 1.567 | 10.579 | 1.218 | 0.998 | 3.298 |
| | Transformer | 1.845 | 1.514 | 9.757 | 1.835 | 1.509 | 9.663 | 1.313 | 1.103 | 4.964 |
| | TCN | 2.029 | 1.610 | 13.760 | 2.082 | 1.623 | 15.219 | 1.375 | 1.163 | 4.510 |
| | BiLSTM + UKF | 1.766 | 1.497 | 9.901 | 1.720 | 1.453 | 9.906 | 1.142 | 0.924 | 5.749 |
| | Proposed | **1.210** | **1.053** | **4.934** | **1.185** | **1.044** | **4.834** | **0.756** | **0.581** | **2.914** |

TABLE III
THE FLOPs, NUMBER OF PARAMETERS, AND INFERENCE TIME OF THE JOINT ESTIMATION METHODS

| Model | N-BEATS | Transformer | TCN | BiLSTM + UKF | Proposed |
|---|---|---|---|---|---|
| FLOPs | 15,558,127 | 3,948,363 | 7,421,199 | 49,795 | 41,931,785 |
| Parameters | 7,788,779 | 266,883 | 117,379 | 109,251 | 197,786 |
| Time (ms) | 110.884 | 100.195 | 114.509 | 316.321 | 32.204 |

TABLE IV
STANDARD DEVIATION SETTINGS FOR DIFFERENT NOISE LEVELS.

| Noise | 1 | 2 | 3 | 4 | 5 | 6 |
|---|---|---|---|---|---|---|
| $\sigma_i$ | 0 | 0.00005 | 0.0001 | 0.0002 | 0.0003 | 0.0004 |
| $\sigma_v$ | 0 | 0.01 | 0.04 | 0.06 | 0.1 | 0.14 |
| $\sigma_t$ | 0 | 0.05 | 0.10 | 0.15 | 0.2 | 0.25 |

followed the ground truth, maintaining an error within 2.0% throughout the cycle.

The SOH estimation results are presented in Fig.11. The SOH predicted by the proposed framework closely align with

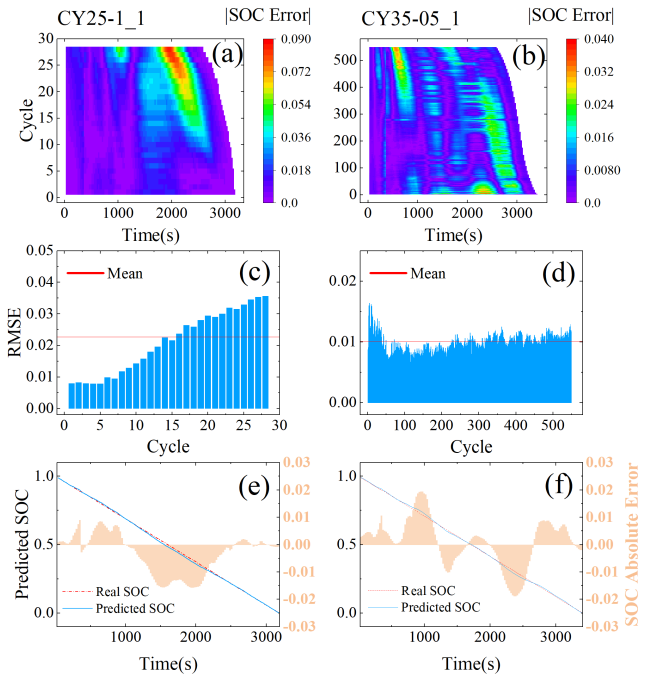


Fig. 10. SOC estimation results on Dataset 2: (a)–(b) absolute errors for "CY25-1_1" and "CY35-05_1"; (c)–(d) cycle-wise RMSEs for "CY25-1_1" and "CY35-05_1"; (e)–(f) SOC estimation curves for the first cycle of "CY25-1_1" and "CY35-05_1".

TABLE V
RMSEs, MAEs, AND MAXs OF SOC AND SOH ESTIMATION ON DATASET 2 (IN %).

| Battery | SOC | | | SOH | | |
|---|---|---|---|---|---|---|
| | RMSE | MAE | MAX | RMSE | MAE | MAX |
| CY25-1_1 | 2.27 | 1.59 | 8.57 | 0.84 | 0.69 | 1.83 |
| CY35-05_1 | 1.01 | 0.80 | 3.52 | 1.44 | 1.17 | 2.76 |

the ground truth for both cells. The estimation errors for each cycle were below 2.0% on "CY25-1_1" and below 3.0% on "CY35-05_1".

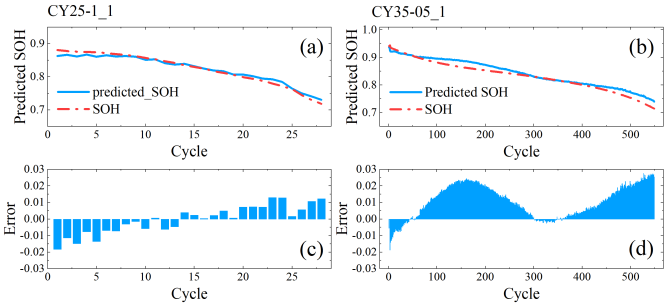


Fig. 11. SOH estimation results on Dataset 2: (a)–(b) SOH estimation curves for "CY25-1_1" and "CY35-05_1"; (c)–(d) SOH estimation errors.

The evaluation metrics for both test cells are summarized in Table V. These experimental results demonstrate that the proposed framework achieved reliable and consistent performance on Dataset 2, further confirming its robustness and superior predictive capability.

## V. CONCLUSION

This paper proposes a CNN-based multi-timescale framework for the joint estimation of SOC, SOE, and SOH for lithium-ion batteries. The framework is designed to account for the distinct temporal and dynamic characteristics of each state by employing dedicated estimation models tailored to their specific behaviors. Moreover, it incorporates targeted update strategies for each state, thereby achieving an effective balance between computational efficiency and estimation accuracy. Experimental validation demonstrates that the proposed joint estimation framework achieves high accuracy, with the RMSEs of SOC, SOE, and SOH all below 1.3%, 1.3%, and 1%, respectively. Compared with several single-state and multi-state estimation models, the proposed framework provides more accurate predictions of SOC, SOE, and SOH in most cases. Further experiments indicate that incorporating degradation factors during the battery aging stage reduces the RMSEs of SOC and SOE estimation by 55.76% and 61.59%, respectively. Moreover, when noise is introduced into the input data, the framework demonstrates stronger robustness against interference compared with other models. It also yields reliable results across datasets collected under multiple temperature conditions. The proposed framework, relying on universal measurements, shows potential for generalization across battery types, and future work will focus on integrating few-shot or semi-supervised learning to address data scarcity, enabling accurate SOH estimation with limited degradation data.

## REFERENCES

[1] K. Liu, Z. Wei, C. Zhang, Y. Shang, R. Teodorescu, and Q.-L. Han, "Towards long lifetime battery: Ai-based manufacturing and management," *IEEE/CAA Journal of Automatica Sinica*, vol. 9, no. 7, pp. 1139–1165, 2022.

[2] K. Li, F. Wei, K. J. Tseng, and B.-H. Soong, "A practical lithium-ion battery model for state of energy and voltage responses prediction incorporating temperature and ageing effects," *IEEE Transactions on Industrial Electronics*, vol. 65, no. 8, pp. 6696–6708, 2017.

[3] X. Hu, F. Feng, K. Liu, L. Zhang, J. Xie, and B. Liu, "State estimation for advanced battery management: Key challenges and future trends," *Renewable and Sustainable Energy Reviews*, vol. 114, p. 109334, 2019.

[4] K. Luo, X. Chen, H. Zheng, and Z. Shi, "A review of deep learning approach to predicting the state of health and state of charge of lithium-ion batteries," *Journal of Energy Chemistry*, vol. 74, pp. 159–173, 2022.

[5] Y. Wang, J. Tian, Z. Sun, L. Wang, R. Xu, M. Li, and Z. Chen, "A comprehensive review of battery modeling and state estimation approaches for advanced battery management systems," *Renewable and Sustainable Energy Reviews*, vol. 131, p. 110015, 2020.

[6] Z. Cui, L. Kang, L. Li, L. Wang, and K. Wang, "A hybrid neural network model with improved input for state of charge estimation of lithium-ion battery at low temperatures," *Renewable Energy*, vol. 198, pp. 1328–1340, 2022.

[7] J. Chen, Y. Zhang, J. Wu, W. Cheng, and Q. Zhu, "Soc estimation for lithium-ion battery using the lstm-rnn with extended input and constrained output," *Energy*, vol. 262, p. 125375, 2023.

[8] L. Ma, C. Hu, and F. Cheng, "State of charge and state of energy estimation for lithium-ion batteries based on a long short-term memory neural network," *Journal of Energy Storage*, vol. 37, p. 102440, 2021.

[9] Y.-X. Wang, Z. Chen, and W. Zhang, "Lithium-ion battery state-of-charge estimation for small target sample sets using the improved gru-based transfer learning," *Energy*, vol. 244, p. 123178, 2022.

[10] B. Yang, Y. Qian, Q. Li, Q. Chen, J. Wu, E. Luo, R. Xie, R. Zheng, Y. Yan, S. Su *et al.*, "Critical summary and perspectives on state-of-health of lithium-ion battery," *Renewable and Sustainable Energy Reviews*, vol. 190, p. 114077, 2024.

[11] B. Jiang, J. Zhu, X. Wang, X. Wei, W. Shang, and H. Dai, "A comparative study of different features extracted from electrochemical impedance spectroscopy in state of health estimation for lithium-ion batteries," *Applied Energy*, vol. 322, p. 119502, 2022.

[12] P. Wen, Z.-S. Ye, Y. Li, S. Chen, P. Xie, and S. Zhao, "Physics-informed neural networks for prognostics and health management of lithium-ion batteries," *IEEE Transactions on Intelligent Vehicles*, vol. 9, no. 1, pp. 2276–2289, 2023.

[13] J. Wen, X. Chen, X. Li, and Y. Li, "Soh prediction of lithium battery based on ic curve feature and bp neural network," *Energy*, vol. 261, p. 125234, 2022.

[14] F. Liu, D. Yu, C. Shao, X. Liu, and W. Su, "A review of multi-state joint estimation for lithium-ion battery: Research status and suggestions," *Journal of Energy Storage*, vol. 73, p. 109071, 2023.

[15] Y. Li, K. Li, X. Liu, X. Li, L. Zhang, B. Rente, T. Sun, and K. T. Grattan, "A hybrid machine learning framework for joint soc and soh estimation of lithium-ion batteries assisted with fiber sensor measurements," *Applied Energy*, vol. 325, p. 119787, 2022.

[16] Y. Song, D. Liu, H. Liao, and Y. Peng, "A hybrid statistical data-driven method for on-line joint state estimation of lithium-ion batteries," *Applied Energy*, vol. 261, p. 114408, 2020.

[17] T.-E. Fan, S.-M. Liu, X. Tang, and B. Qu, "Simultaneously estimating two battery states by combining a long short-term memory network with an adaptive unscented kalman filter," *Journal of Energy Storage*, vol. 50, p. 104553, 2022.

[18] L. Chen, Y. Song, A. M. Lopes, X. Bao, Z. Zhang, and Y. Lin, "Joint estimation of state of charge and state of energy of lithium-ion batteries based on optimized bidirectional gated recurrent neural network," *IEEE transactions on transportation electrification*, vol. 10, no. 1, pp. 1605–1616, 2023.

[19] C. Qian, H. Guan, B. Xu, Q. Xia, B. Sun, Y. Ren, and Z. Wang, "A cnn-sam-lstm hybrid neural network for multi-state estimation of lithium-ion batteries under dynamical operating conditions," *Energy*, vol. 294, p. 130764, 2024.

[20] J. Tian, R. Xiong, J. Lu, C. Chen, and W. Shen, "Battery state-of-charge estimation amid dynamic usage with physics-informed deep learning," *Energy Storage Materials*, vol. 50, pp. 718–729, 2022.

[21] J. H. Andrews and R. F. Harris, "r-and k-selection and microbial ecology," in *Advances in microbial ecology*, pp. 99–147. Springer, 1986.

[22] J. Zhu, Y. Wang, Y. Huang, R. Bhushan Gopaluni, Y. Cao, M. Heere, M. J. Mühlbauer, L. Mereacre, H. Dai, X. Liu *et al.*, "Data-driven capacity estimation of commercial lithium-ion batteries from voltage relaxation," *Nature communications*, vol. 13, no. 1, p. 2261, 2022.

[23] L. R. Medsker, L. Jain *et al.*, "Recurrent neural networks," *Design and Applications*, vol. 5, no. 64-67, p. 2, 2001.

[24] B. N. Oreshkin, D. Carpov, N. Chapados, and Y. Bengio, "N-beats: Neural basis expansion analysis for interpretable time series forecasting," *arXiv preprint arXiv:1905.10437*, 2019.

[25] K. Han, Y. Wang, H. Chen, X. Chen, J. Guo, Z. Liu, Y. Tang, A. Xiao, C. Xu, Y. Xu *et al.*, "A survey on vision transformer," *IEEE transactions on pattern analysis and machine intelligence*, vol. 45, no. 1, pp. 87–110, 2022.

[26] Y. Liu, H. Dong, X. Wang, and S. Han, "Time series prediction based on temporal convolutional network," in *2019 IEEE/ACIS 18th International conference on computer and information science (ICIS)*, pp. 300–305. IEEE, 2019.

[27] S. Siami-Namini, N. Tavakoli, and A. S. Namin, "The performance of lstm and bilstm in forecasting time series," in *2019 IEEE International conference on big data (Big Data)*, pp. 3285–3292. IEEE, 2019.

[28] P. Li, J. Ye, J. Hou, Z. Deng, and S. Xiang, "State of charge estimation for lithium-ion battery using a multi-feature mamba network and ukf under mixed operating conditions," *Energy*, p. 137539, 2025.

[29] P. Guo, W. Ma, X. Liu, and B. Chen, "Robust model parameter identification and soc estimation for li-ion batteries considering noisy measurement," *IEEE Transactions on Industrial Electronics*, 2025.


**Yihuan Li** received the Ph.D. degree in Electronic and Electrical Engineering from the University of Leeds, U.K., in 2021. She is currently a Lecturer at North China Electric Power University, Beijing, China. Her research interests include intelligent modeling, monitoring and control, and their applications to energy storage systems.

**Kaituo Liu** was born in China in 2001. He received the B.S. degree in robotic engineering from Nanjing University of Information Science and Technology, Nanjing, China, in 2023. He is currently pursuing the M.S. degree in control science and engineering at North China Electric Power University, Beijing, China. His research interests include battery state monitoring and machine learning.

**Wei Wang** was born in China in 1986. He received the Ph.D. degree in control theory and control engineering from North China Electric Power University, Beijing, China, in 2011. He is currently a Professor with the State Key Laboratory of Alternate Electrical Power System with Renewable Energy Sources, North China Electric Power University. His research interests mainly include the modeling, optimization and control of integrated energy system.

**Fang Fang** (Senior Member, IEEE) received the Ph.D. degree in thermal power engineering from North China Electric Power University, Beijing, China, in 2005. His current research interests include the modeling and control of power generation units, the configuration and operation of integrated energy systems, and the optimal dispatching of virtual power plants. Prof. Fang is the Chair of China Energy Research Society Technical Committee on Smart Power Generation and a Council Member of the Technical Committee on Industrial Information Physical Systems, IEEE Industrial Electronics Society.

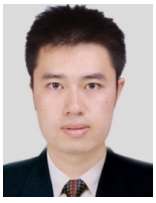

**Kailong Liu** (Senior Member, IEEE) is a Professor at the Shenzhen Research Institute of Shandong University, Shenzhen, China. He received the Ph.D. degree in electrical engineering from Queen's University Belfast, UK, in 2018. His research interests include modeling, optimization and control with applications to electric vehicles, energy storage, battery manufacture and management.

**Kang Li** (Senior Member, IEEE) received the B.Sc. degree from Xiangtan University, Xiangtan, Hunan, China, in 1989, the M.Sc. degree from Harbin Institute of Technology, Harbin, China, in 1992, and the Ph.D. degree from Shanghai Jiao Tong University, Shanghai, China, in 1995. His current research interests include nonlinear system modeling, identification and controls, bioinspired computational intelligence, and fault diagnosis and detection.